Non-linear modelling of a high speed railway pantograph with parameter optimisation

J. Gil[a,*], M. Tur[a], A. Correcher[b], S. Gregori[a], A. Pedrosa[a], F.J. Fuenmayor[a]

[a] *Instituto de Ingeniería Mecánica y Biomecánica, Universitat Politècnica de València, Camino de Vera s/n, 46022, Valencia (Spain)*
[b] *Instituto de Automática e Informática Industrial, Universitat Politècnica de València, Camino de Vera s/n, 46022, Valencia (Spain)*

Abstract

The accuracy of the pantograph model is crucial for the reliability of any pantograph-catenary simulation. Pantograph non-linearities make very challenging the design of a model and the selection of a proper parametric representation to fit the experimental data. This work proposes a novel pantograph non-linear model including three-part oblique springs with dry friction for accurately emulating the behaviour of the DSA 380 pantograph. Furthermore, an efficient method of integrating Coulomb friction is employed successfully as a result of a proposed strategy. A genetic algorithm is employed to optimise the parameters of the model and achieve a good agreement with the experimental data. The resulting optimised model shows a very similar behaviour with the real pantograph also for data not included in the optimisation.

Keywords: Non-linear dynamics, Pantograph model, Catenary, Coulomb friction, Parameter optimisation

*Corresponding author.
Email address: jaigiro@upv.es (J. Gil)

1. Introduction

The pantograph catenary interaction is the object of study of multiple researchers [1] whose objective is a more reliable and accurate representation of the whole system. Nowadays the validity of the pantograph-catenary simulations rely on the capacity of the software to pass the requirements of the European Standard EN 50318 [2]. However this Standard is particularly designed to the validation of the catenary models and it only includes a procedure for the validation of pantograph models where the accuracy is assessed with a frequency response function where non-linear features are not properly considered, furthermore, only a centred force is contemplated.

Thus a novel technique of Hybrid Simulation of Hardware In the Loop (HIL) has been arising as an alternative [3, 4, 5, 6, 7] where pantograph models are not required and virtual catenary interacts with real pantographs, bypassing in this way the need of a pantograph model.

In this work we are interested in using a pantograph test rig to collect data of a particular pantograph (DSA 380) and generates a pantograph model. This model has to be able to explain the non-linear behaviour observed in the pantograph and reproduce accurately the collected data.

The most common pantograph models used in the literature are the lumped mass models [8] that emulates the basis of the pantograph linear dynamics under 20 Hz. For modelling higher frequency content is important to consider the elasticity of the pantograph contact strips, as in the multi-mass system of [9], which also includes the wear profile of the contact strip.

In [10] the non-linear behaviour of pantograph damper is considered in the formulation as an important part of a rigid multi-body pantograph. Other well known class of pantograph models are the flexible multi-body as the presented in [11]. Sometimes the parameter identification is very important for the accuracy of the pantograph model, in [12] the different parts of the pantograph are disassembled and tested to obtain the inertia an dissipative parameters. The model itself is formed by a rigid linkage combined with elastic and viscoelastic elements. The overall performance of the pantograph is tested with the whole system assembled but only in a test with a unit-step load in which the pantograph reach the equilibrium position after 5 seconds. In [13] A flexible multi-body pantograph system incorporates an non ideal joint that allows relative displacement at the joint. Another aspects that can be modelled in pantograph is the external aerodynamics forces. In [14] a detailed guide to incorporate aerodynamic forces on the pantograph components and the influence of those on the contact force are displayed.

There is no general procedure to obtain non-linear models and every system has its own particularities. The contribution of this paper is the particular strategy proposed to model the DSA380 pantograph. A specific non-linear element formed by a oblique spring with dry friction has been identified as the main source of non-linearities and the dynamic behaviour of this element is studied. The parametric representation of the model has succeeded in fitting the collected data of the pantograph by the use of a genetic algorithm. Another contribution of this paper is the strategy followed to integrate Coulomb friction by modifying the tangent matrix in the Newton-Raphson method.

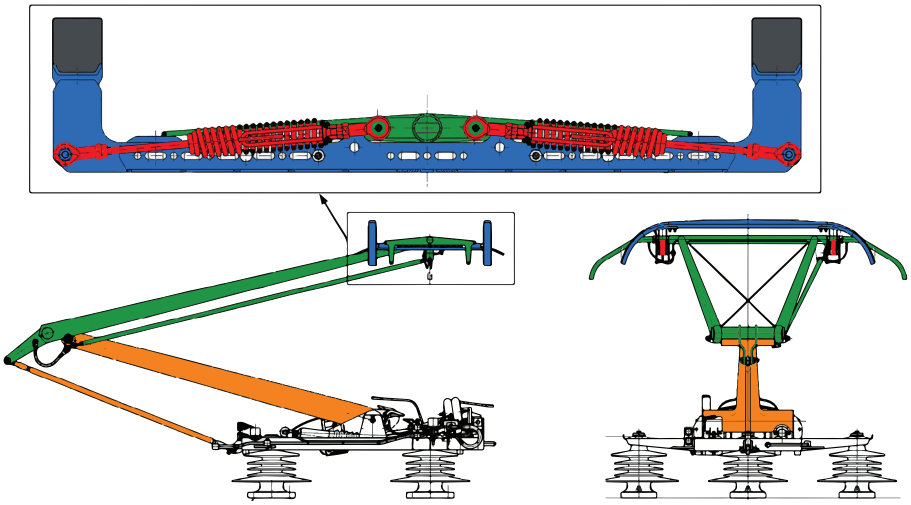


Figure 1: *DSA 380 pantograph.*

In section 2 the non-linear behavior of the pantograph is analysed. Then in Section 3 the pantograph model is presented. In section 4 the parameter optimisation is conducted to fit the pantograph data and the conclusions are confined to Section 5.

2. Non-linear behavior of the DSA 380 pantograph

DSA 380 pantograph is a linkage designed to contact the catenary contact wire and has different parts as seen in Fig. 1. The pantograph head (blue) is formed by two contact strips which hang over four oblique springs (red) that connect it with the upper frame (green) and the lower frame (orange).

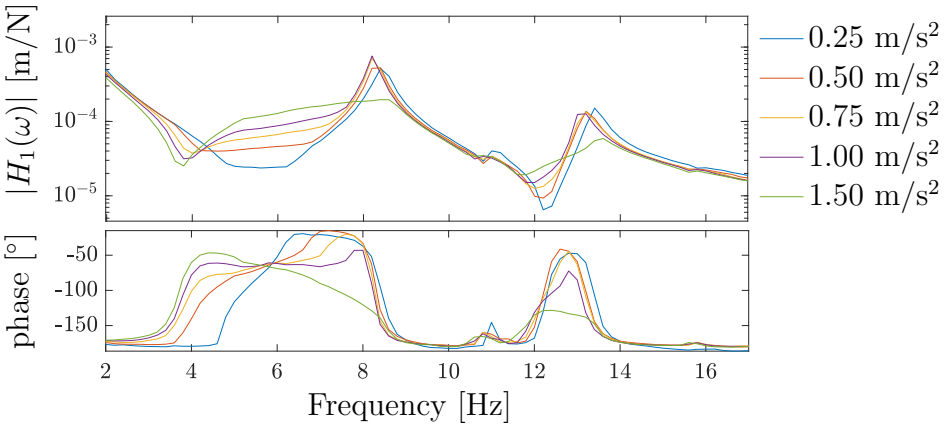
2.1. Frequency response function

The dynamics of the pantograph is often described with the Frequency Response Function (FRF) that relates the vertical displacement of the pantograph head with the contact force applied. This analysis must be employed

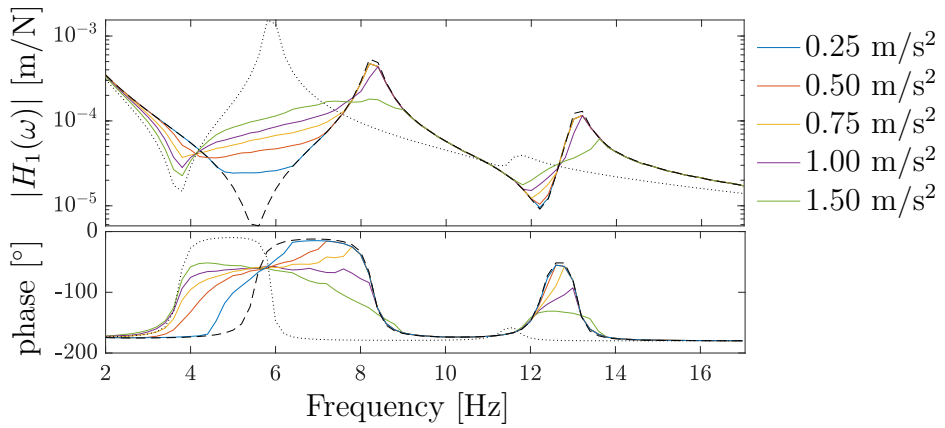
with linear models so there is independence between the different frequencies of the spectrum and the FRF is unique. However, non-linear Frequency Response Analysis (NFRA) can be very useful to understand non-linear systems and evaluate the grade of non-linearity. In non-linear systems, a first-order frequency response function $H_1(\omega)$ can be defined as the spectral ratio of the response to the force at the excitation frequency ω while all the other harmonic components are ignored. The first-order FRF is not unique and depends on the amplitude of the response and, in general, on all the features of the excitation applied. In this work, the sinusoidal excitation technique is employed and the pantograph is excited with single-frequency displacement signals, and $H_1(\omega)$ is computed neglecting the force frequency content that is not excited. As proof of the non-linearity of the system, Fig. 2 (a) shows the different firs-order FRFs obtained with the DSA 380 pantograph when imposing sinusoidal displacements with different amplitudes. The non-linearity is pointed out by the existence of multiple curves and how much they differ, especially in certain frequency ranges.

2.2. Z-spring

The first attempt to describe mathematically the pantograph behaviour is to use a linear pantograph model as the conventional lumped mass model shown in Fig. 3 (a). Every part of the model is coloured accordingly to the pantograph parts and notice that the stiffness k_1^{eq} represents the contribution of the four oblique springs. The FRF of this linear model is unique so there is no chance of reproducing the behaviour observed in Fig. 2 (a) but the parameters of the model (mass, stiffness and damping coefficients) can be tuned or optimised to fit every curve separately, that is, a different model



(a) *Measurements of the DSA 380 model.*



(b) *Simulations of the three degrees of freedom with Z-spring model (coloured lines), linear model 1 (dashed line) and linear model 2 (dotted line).*

Figure 2: *First-order FRF for different excitation amplitudes.*

for every different FRF curve. This strategy is evidently not great for two reasons. First, you have a different model for every amplitude and they are only valid for sinusoidal scenario. Second, the fit of every individual curve is not great, especially for the 1.50 m/s^2 curve, which does not look like the FRF of a linear dynamic model. However, a remarkable fact has been noticed: the adjusted values of k_1^{eq} are much higher (about 12000 N/m on average) than the value measured statically in the pantograph (about 6000 N/m). This incongruity cannot be explained with the non-linear behaviour of an oblique pre-stressed spring and it is the starting point to understand the non-linearity of the pantograph behaviour.

The solution lies in the topology of the pantograph head springs. Every one of the four springs that can be observed in red in Fig. 1 is actually formed by two rigid bars connected by revolution joints and a pre-stressed spring which connects both bars. This configuration is going to be called Z-spring due to the three pieces involved. This system behaves differently to an oblique spring due to the friction present in the two joints. In Fig. 4 the configuration of one single Z-spring model is shown and the friction moment at joints. This Z-spring model has a complex behaviour but when the amplitude of the movement is small the friction is strong enough to block the bars and it moves as shown in Fig. 5 (a). This mode of functioning corresponds to a higher stiffness as obtained in most of the adjusted k_1^{eq} with the FRF curves. However for bigger amplitudes, the friction is negligible and the Z-spring moves as shown in Fig. 5 (b), which corresponds with a smaller stiffness, as observed when measuring it statically (great amplitudes were applied). This explains the different estimations of the stiffness done

previously.

After noticing that the Z-spring can be responsible for the non-linear behaviour, its influence in the first-order FRF is going to be evaluated. Fig. 3 (b) shows a conventional lumped mass model where the linear spring is replaced by a Z-spring that, in this case, represents the four oblique springs of the real pantograph. In Fig. 2 (b) the first-order FRF's of this model are shown for different amplitudes of excitation (acceleration amplitude of the displacement imposed). This model is able to exhibit the same kind of first-order FRF's observed in the pantograph (Fig. 2 (a)). Furthermore, this 3 d.o.f. model with Z-spring can be linearised around two functioning points in order to understand its behaviour. Let us define the linear model 1 as the model linearized around the equilibrium point considering that friction does not allow the joints of the Z-srping to rotate as in Fig. 5 (a). Additionally, the linear model 2 is the model linearised around the equilibrium point when friction is negligible compared with other forces and the movement of the Z-spring can be observed in 5 (b). In Fig. 2 (b) both linearised models are plotted in black and it can be observed that the behaviour of the non-linear model is bounded by both linearised models.

3. Pantograph Model

In the previous section it has been seen that the dynamic behaviour of the Z-spring explain the main non-linear features observed in the pantograph measurements. In this section a more complex pantograph model that accounts for the bending of the pantograph head, the asymmetry of the pantograph and the roll of the pantograph head and upper frame is described

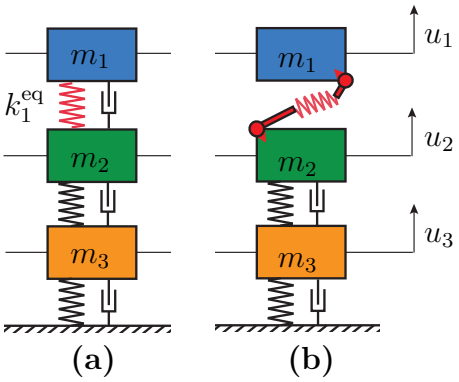


Figure 3: *(a) Three degree of freedom linear model and (b) three degree of freedom model with Z-spring.*

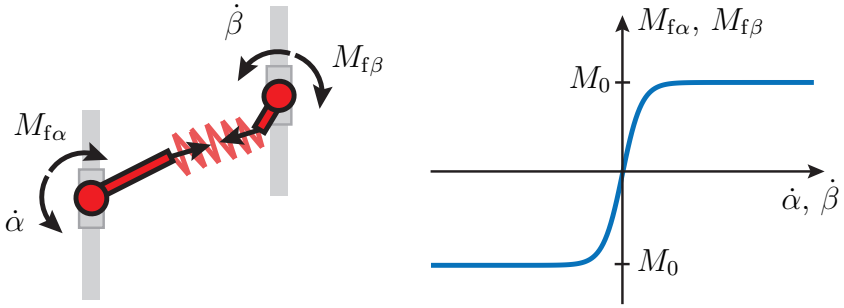


Figure 4: *Z-spring configuration and friction at the two joints.*

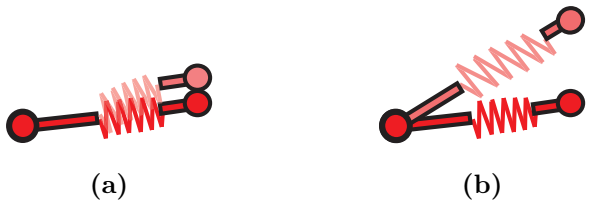


Figure 5: *Z-spring movement when (a) friction block the bars and (b) friction is negligible.*

topologically and mathematically.

3.1. Description

Looking at the pantograph (Fig. 1) there are certain features that are included in the pantograph model of Fig. 6:

- The bending stiffness of the pantograph strips: the two contact strips are considered as a single beam (blue) since it is assumed that the movement of both is the same. A point mass at every side emulates the weight of the remaining parts of the pantograph head.

- Two Z-springs (red), each representing the two symmetric oblique springs of every side of the pantograph. Since every Z-spring represents two of the real ones, there is no moment transmitted to the pantograph head or upper frame due to symmetry.

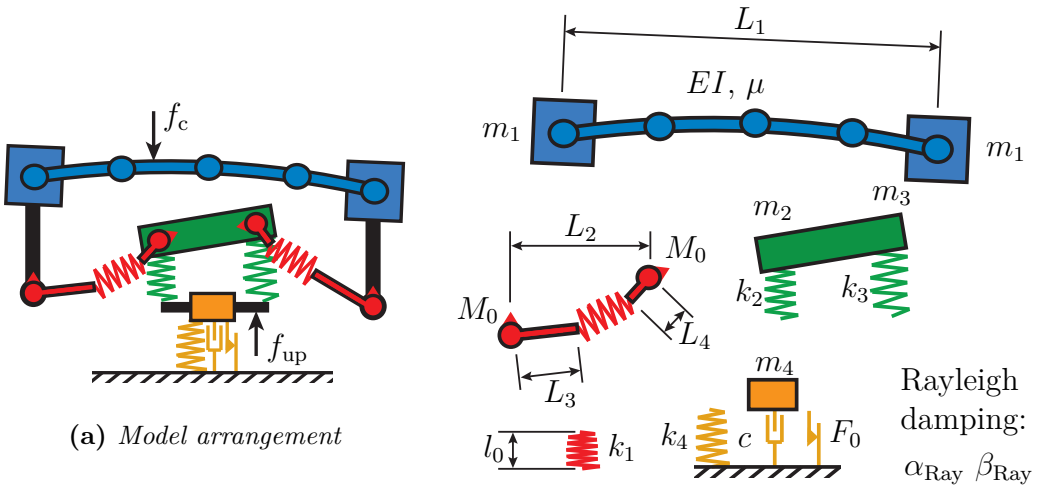
- The upper frame (green) allows the roll movement and it accounts for the asymmetric bar on the right of the pantograph (Fig. 1) by considering different mass and stiffness in both sides.

- The lower frame (orange) considers coulomb friction and a damper.

Over this model there is three forces acting: the contact force on the pantograph head f_{c}, the uplift mechanism force f_{up} and the weight. The parameters defining the geometric and mechanical properties can be seen in Fig. 6 (b) and are defined in Tab. 1. The values of the parameters shown in the table are obtained by a optimisation performed in Section 4.

Table 1: *Parameters of the model. Optimised parameters are marked with a* $\times$*.*

m_1	Pantograph head lateral mass	$\times$	2.36 kg
EI	Pantograph head bending stiffness	$\times$	6196.6 Nm^2
μ	Pantograph head linear density	$\times$	3.46 kg/m
L_1	Pantograph head length		86 cm
L_2	Z-spring fixed horizontal length		26 cm
L_3	Z-spring bar length		11.98 cm
L_4	Z-spring bar length		5.98 cm
M_0	Z-spring joint Coulomb friction (2x)	$\times$	0.42 Nm
l_0	Z-spring undeformed length	$\times$	6.24 cm
k_1	Z-spring stiffness (2x)	$\times$	30769 N/m
m_2	Upper frame left mass	$\times$	3.79 m
m_3	Upper frame right mass	$\times$	3.66 m
k_2	Upper frame left stiffness	$\times$	24597.6 N/m
k_3	Upper frame right Stiffness	$\times$	27201.9 N/m
m_4	Lower frame mass	$\times$	4.49 kg
k_4	Lower frame stiffness	$\times$	305.54 N/m
c	Lower frame damping coefficient	$\times$	21.9 Ns/m
F_0	Lower frame Coulomb friction	$\times$	0.43 N
α_{Ray}	Rayleigh damping coefficient	$\times$	0.147 s^{-1}
β_{Ray}	Rayleigh damping coefficient	$\times$	5.36 10^{-4} s
Δt	Time increment		2 ms
α	Numerical damping HHT		0.3
k	Coulomb regularisation: $\tanh k\dot{\alpha}$		1000



(a) *Model arrangement*

(b) *Parametres of the model*

Figure 6: *Description of the non-linear pantograph model with geometric and mechanical properties.*

3.2. Mathematical representation

The degrees of freedom are indicated in Fig. 7 and collected in in a vector:

$$\mathbf{u} = [u_1 \;\; \theta_1 \;\; u_2 \;\; \theta_2 \;\; u_3 \;\; \theta_3 \;\; u_4 \;\; \theta_4 \;\; u_5 \;\; \theta_5 \;\; \alpha_1 \;\; \alpha_2 \;\; \beta_1 \;\; \beta_2 \;\; u_6 \;\; u_7 \;\; u_8]^\top \quad (1)$$

The dynamic equation that suits this non-linear model with Coulomb friction has this form:

$$\mathbf{M}\ddot{\mathbf{u}} + \mathbf{C}\dot{\mathbf{u}} + \mathbf{F}^{\mathrm{e}}(\mathbf{u}) + \mathbf{F}^{\mathrm{f}}(\dot{\mathbf{u}}) = \mathbf{F} \quad (2)$$

where $\mathbf{M}$ is the mass global matrix, $\mathbf{C}$ is the damping global matrix, $\mathbf{F}^{\mathrm{e}}$ is the elastic generalised forces in degrees of freedom, $\mathbf{F}^{\mathrm{f}}$ Coulomb friction generalised forces and $\mathbf{F}$ the external forces including the contact force f_c, the uplift force of the pressure system f_{up} and the weight. Different parts

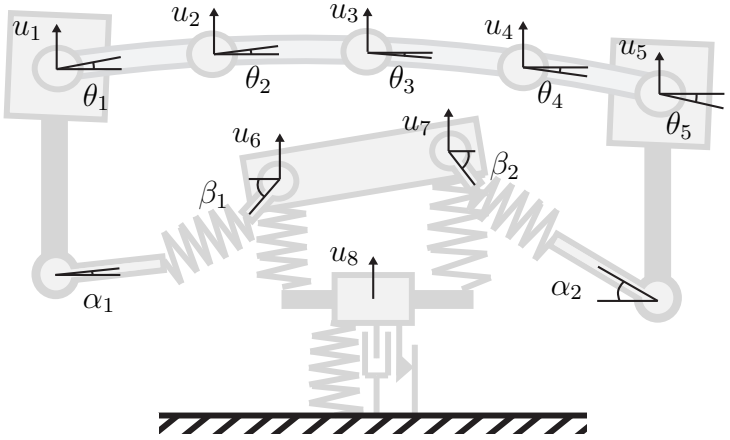


Figure 7: *Description of the degrees of freedom of the pantograph model.*

of the model contribute to the elastic forces $\mathbf{F}_{\mathrm{e}}$, some of them have a linear formulation and others do not, thus, the elastic forces can be expressed as:

$$\mathbf{F}^{\mathrm{e}} = \mathbf{F}^{\mathrm{eNL}} + \mathbf{K}^{\mathrm{L}}\mathbf{u} \tag{3}$$

where $\mathbf{F}^{\mathrm{eNL}}$ is the elastic forces of non-linear elements (Z-springs) and $\mathbf{K}^{\mathrm{L}}$ is the stiffness matrix that only considers linear elements (pantograph head, lower frame and upper frame).

The different matrices and vectors of (2) are obtained by assembling the contribution of the different parts of the model according to its specific formulation:

The pantograph head is modelled with an Euler-Bernoulli beam formulation and concentrated masses at both sides. Mass $\mathbf{M}$ and stiffness $\mathbf{K}^{\mathrm{L}}$ matrices are well known and are assembled in the system global size. The damping matrix of this part is computed according to Rayleigh damping $\mathbf{C} = \alpha_{\mathrm{Ray}}\mathbf{M} + \beta_{\mathrm{Ray}}\mathbf{K}^{\mathrm{L}}$.

Each of the two Z-springs is formed by two rigid bars and a spring. The spring is a non-linear element and the elastic forces associated with it can be computed by deriving the potential energy with respect to the degrees of freedom according to the Euler-Lagrange equation. For example, for the left Z-spring:

$$E_{\mathrm{p}} = \frac{1}{2} k_1 (l - l_0)^2 \tag{4}$$

where the deformed length of the spring is:

$$\begin{aligned} & l = \sqrt{(L_3 \mathrm{C}_{\alpha_1} + L_4 \mathrm{C}_{\beta_1} - L_2)^2 + (-L_3 \mathrm{S}_{\alpha_1} - L_4 \mathrm{S}_{\beta_1} + u_6 - u1)^2} \\ & \mathrm{C}_{\alpha_1} = \cos \alpha_1;\ \mathrm{S}_{\alpha_1} = \sin \alpha_1;\ \mathrm{C}_{\beta_1} = \cos \beta_1;\ \mathrm{S}_{\beta_1} = \sin \beta_1 \end{aligned} \tag{5}$$

From where it is obtained the elastic forces (only the contribution of the left Z-spring) generalised at the degrees of freedom u_1,u_6, α_1 and β_1 are obtained:

$$\mathbf{F}^{\mathrm{eNL}} = \frac{2k_1(l - l_0)}{l} \begin{bmatrix} u_1 - u_6 + L_4 \mathrm{S}_{\beta_1} + L_3 \mathrm{S}_{\alpha_1} \\ L_4 \mathrm{C}_{\beta_1}(u_1 - u_6 + L_4 \mathrm{S}_{\beta_1} + L_3 \mathrm{S}_{\alpha_1}) - L_4 \mathrm{S}_{\beta_1}(L_4 \mathrm{C}_{\beta_1} - L_2 + L_3 \mathrm{C}_{\alpha_1}) \\ L_3 \mathrm{C}_{\alpha_1}(u_1 - u_6 + L_4 \mathrm{S}_{\beta_1} + L_3 \mathrm{S}_{\alpha_1}) - L_3 \mathrm{S}_{\alpha_1}(L_4 \mathrm{C}_{\beta_1} - L_2 + L_3 \mathrm{C}_{\alpha_1}) \\ -(u_1 - u_6 + L_4 \mathrm{S}_{\beta_1} + L_3 \mathrm{S}_{\alpha_1}) \end{bmatrix} \tag{6}$$

In the Z-spring there is also Coulomb friction at the two revolution joints (see Fig. 4). The maximum friction allowed is the parameter M_0 at every joint and the friction force vector is a function of the velocity of the degree of freedom affected. The hyperbolic tangent function is used to regularise the Coulomb law, so the friction generalised force at the degrees of freedom α_1 and β_1 is:

$$\mathbf{F}^{\mathrm{f}} = M_0 \begin{bmatrix} \tanh k\dot{\alpha_1} \\ \tanh k\dot{\beta_1} \end{bmatrix} \tag{7}$$

where k defines how abrupt is the change of the friction between M_0 and $-M_0$. Higher values of k stand for a more accurate representation of the Coulomb law but in exchange for numerical stability. A value of $k = 1000$ has experimentally been demonstrated to be big enough for the convergence of the simulations performed in this work.

The two remaining parts of the model are the upper and lower frames. The mass and stiffness matrices that include the contribution of these two parts related to the degrees of freedom u_6, u_7 and u_8 are:

$$\mathbf{M} = \begin{bmatrix} m_2 & 0 & 0 \\ 0 & m_3 & 0 \\ 0 & 0 & m_4 \end{bmatrix}; \quad \mathbf{K}^{\mathrm{L}} = \begin{bmatrix} k_2 & 0 & -k_2 \\ 0 & k_3 & -k_3 \\ -k_2 & -k_3 & k_2 + k_3 + k_4 \end{bmatrix} \tag{8}$$

and the damping matriz related to the same three degrees of freedom is:

$$\mathbf{C} = \begin{bmatrix} 0 & 0 & 0 \\ 0 & 0 & 0 \\ 0 & 0 & c \end{bmatrix} + \alpha_{\mathrm{Ray}}\mathbf{M} + \beta_{\mathrm{Ray}}\mathbf{K}^{\mathrm{L}} \tag{9}$$

The friction generalised force at the degree of freedom u_8 is:

$$F^{\mathrm{f}} = F_0 \tanh k u_8 \tag{10}$$

In the tests conducted with the pantograph (see Fig. 9) the actuator imposes a displacement signal at one point of the pantograph head (actually two points, one at every contact strip, but are considered as a single point in the model) and the total force between the actuator and the pantograph is measured. Thus the same scheme is followed to simulate the model: the displacement of a point of the pantograph head is imposed and the output

of the simulation is the resulting force at that point. Assuming that the displacement is imposed at a node of the pantograph head so we can directly restrict a degree of freedom, all the degrees of freedom $\mathbf{u}$ can be divided into free $\mathbf{u}_\mathrm{a}$ and constrained u_b so (2) can be expressed as:

$$\begin{bmatrix} \mathbf{M}_{\mathrm{aa}} & \mathbf{M}_{\mathrm{ab}} \\ \mathbf{M}_{\mathrm{ba}} & M_{\mathrm{bb}} \end{bmatrix} \begin{Bmatrix} \ddot{\mathbf{u}}_\mathrm{a} \\ \ddot{u}_\mathrm{b} \end{Bmatrix} + \begin{bmatrix} \mathbf{C}_{\mathrm{aa}} & \mathbf{C}_{\mathrm{ab}} \\ \mathbf{C}_{\mathrm{ba}} & C_{\mathrm{bb}} \end{bmatrix} \begin{Bmatrix} \dot{\mathbf{u}}_\mathrm{a} \\ \dot{u}_\mathrm{b} \end{Bmatrix} + \begin{bmatrix} \mathbf{K}_{\mathrm{aa}} & \mathbf{K}_{\mathrm{ab}} \\ \mathbf{K}_{\mathrm{ba}} & K_{\mathrm{bb}} \end{bmatrix} \begin{Bmatrix} \mathbf{u}_\mathrm{a} \\ u_\mathrm{b} \end{Bmatrix} + \\ + \begin{Bmatrix} \mathbf{f}_\mathrm{a}^{\mathrm{eNL}}(\mathbf{u}_\mathrm{a}, u_\mathrm{b}) \\ f_\mathrm{b}^{\mathrm{eNL}}(\mathbf{u}_\mathrm{a}, u_\mathrm{b}) \end{Bmatrix} + \begin{Bmatrix} \mathbf{F}_\mathrm{a}^{\mathrm{f}}(\dot{\mathbf{u}}_\mathrm{a}, \dot{u}_\mathrm{b}) \\ F_\mathrm{b}^{\mathrm{f}}(\dot{\mathbf{u}}_\mathrm{a}, \dot{u}_\mathrm{b}) \end{Bmatrix} = \begin{Bmatrix} \mathbf{F}_\mathrm{a} \\ F_\mathrm{b} \end{Bmatrix} \quad (11)$$

Taking the first row of Eq. (11) we obtain the second-order dynamic equation that allows to solve the unknown $\mathbf{u}_\mathrm{a}$:

$$\mathbf{M}_{\mathrm{aa}}\ddot{\mathbf{u}}_\mathrm{a} + \mathbf{C}_{\mathrm{aa}}\dot{\mathbf{u}}_\mathrm{a} + \mathbf{K}_{\mathrm{aa}}\mathbf{u}_\mathrm{a} + \mathbf{F}_\mathrm{a}^{\mathrm{eNL}}(\mathbf{u}_\mathrm{a}, u_\mathrm{b}) + \mathbf{F}_\mathrm{a}^{\mathrm{f}}(\dot{\mathbf{u}}_\mathrm{a}, \dot{u}_\mathrm{b}) = \mathbf{F}_\mathrm{a} - \mathbf{M}_{\mathrm{ab}}\ddot{u}_\mathrm{b} - \mathbf{C}_{\mathrm{ab}}\dot{u}_\mathrm{b} - \mathbf{K}_{\mathrm{ab}}u_\mathrm{b} \quad (12)$$

where the external force vector $\mathbf{F}_\mathrm{a}$ is produced by the uplift pantograph system with a vertical force at the degree of freedom u_8 and the weight. Solving Eq. (12) is especially challenging due to the non-linear friction and the multiple slip/stick transitions that happen in this problem. In [15] a particular regularization of the Coulomb law and the 4^{th} order Runge-Kuta algorithm is employed for solving efficiently problems with Coulomb friction and slip/stick transitions. We have found that for this case, that strategy needs a very small time step leading to long simulations. Thus we propose to use an implicit integration algorithm, namely the alpha-method HHT (Hilber-Hughes-Taylor) [16] and the Newton-Raphson method to solve the non-linear problem of every time step. However applying straight away HHT and Newton-Raphson has not shown the ability to converge at every time

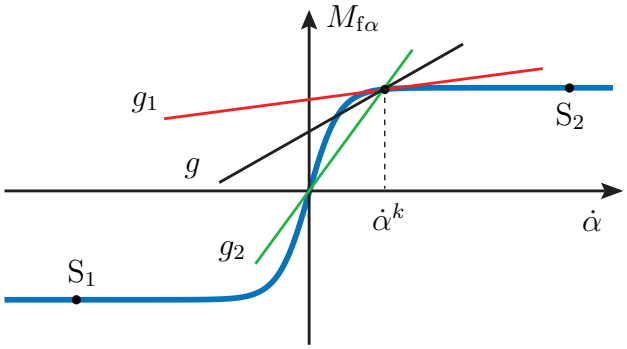


Figure 8: *Regularisation of Coulomb law and modified derivative for improving convergence of Newton-Raphson method.*

step. The iterative Newton-Raphson algorithm tries to find the solution but gets stuck and swings between two states S_1 and S_2 in which the friction has opposite values as shown in Fig. 8. The solution adopted is to modify the tangent matrix by modifying the derivative of the function tanh used in the friction law. If the actual derivative of tanh is:

$$g_1(\dot{\alpha}) = \frac{\mathrm{d}\tanh\dot{\alpha}}{\mathrm{d}\dot{\alpha}} = \mathrm{sech}^2\dot{\alpha} \tag{13}$$

the alternative derivative $g_2(\dot{\alpha})$ is computed as the slope of the line that passes by the origin and the point where the derivative is evaluated (see Fig. 8):

$$g_2(\dot{\alpha}) = \frac{\tanh\dot{\alpha}}{\dot{\alpha}} \tag{14}$$

It has proven to be a valid derivative to solve the convergence issue and additionally the function $g = 0.5g_1 + 0.5g_2$ has shown a faster convergence rate.

This strategy has shown in practise to be much faster than than the 4^{th} order Runge-Kuta method because it allows a much bigger time step for the

same level of accuracy. As a rule of thumb the proposed method get the same accuracy than ODE45 function in Matlab® selecting a time increment 2000 times bigger and employing 250 times less time.

Eq. (12) allows to obtain the free degrees of freedom $\mathbf{u}_\mathrm{a}$ inputing the displacement, velocity and acceleration of the constrained degree of freedom u_b, that can be u_1, u_2, u_3, u_4 or u_5 depending on the excitation point. The second row of Eq. (11) allows to get the reaction force at the node where the displacement is imposed:

$$F_\mathrm{b} = \mathbf{M}_\mathrm{ba}\ddot{\mathbf{u}}_\mathrm{a}+M_\mathrm{bb}\ddot{u}_\mathrm{b}+\mathbf{C}_\mathrm{ba}\dot{\mathbf{u}}_\mathrm{a}+C_\mathrm{bb}\dot{u}_\mathrm{b}+\mathbf{K}_\mathrm{ba}\mathbf{u}_\mathrm{a}+K_\mathrm{bb}u_\mathrm{b}+F_\mathrm{b}^\mathrm{eNL}(\mathbf{u}_\mathrm{a},u_\mathrm{b})+F_\mathrm{b}^\mathrm{f}(\dot{\mathbf{u}}_\mathrm{a},\dot{u}_\mathrm{b}) \tag{15}$$

The reaction force includes the weight and the contact force: $F_\mathrm{b} = -f_\mathrm{c} + W_\mathrm{b}$ so the contact force can be easily computed.

4. Parameter optimisation

In Tab. 1 all the model parameters are listed. Some of them can be measured directly but most of them have to be optimised in order that the model fits the real pantograph behaviour. The optimisation process consists of changing the parameters to reduce the error between the model and the tests following the arrangement of Fig. 9. The actuator follows a desired displacement signal and is connected to the two contact strips in a way that imposes the displacement signal over two points that have the same lateral position. The displacement, velocity and acceleration of the actuator are measured because they are the inputs of the mathematical model. Between the actuator and those two points, there are two force transducers that mea-

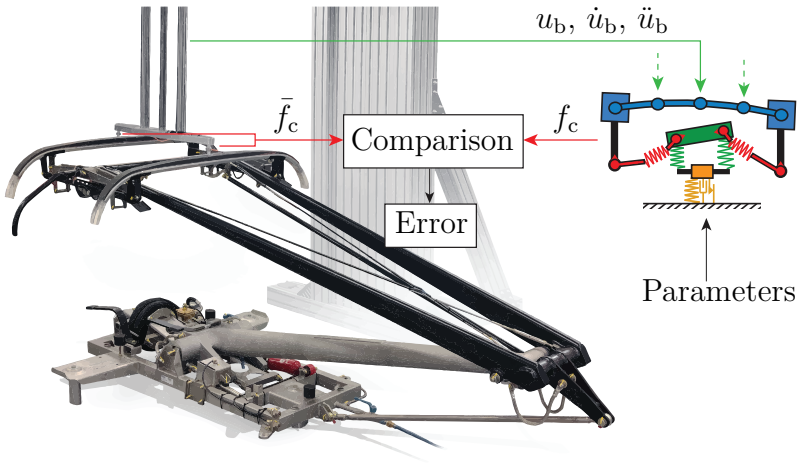


Figure 9: *Pantograph test imposing displacement and obtaining measurement of the force for comparison with simulation.*

sure the total contact force $\bar{f}_c$ obtained from the real pantograph when the displacement is imposed. The actuator can be placed in another position so the load is not centred. The measured contact force can be compared with the force that comes from the mathematical model and the error is computed.

For the tests performed in this work, we are going to impose three different types of signals over the pantograph:

- Chirp signal: the frequency linearly increases with time.
- Pseudo signal: superposition of constant frequency content signal with random phases.
- Catenary signal: displacement of the contact wire extracted from a simulated pantograph-catenary interaction.

For a proper modelling of the pantograph when there is a roll movement of the pantograph head and when the load is not at the centre, the displacement

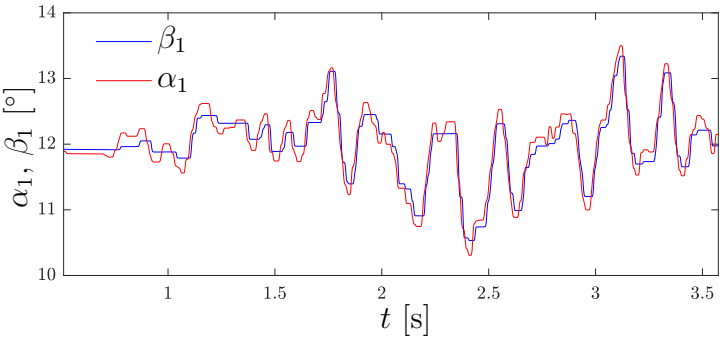


Figure 10: *Simulation of* α_1 *and* β_1

is going to be imposed over three different positions in the pantograph head: centred, on the left and on the right. Those points correspond to the d.o.f. u_3, u_2 or u_4 and the contact force will be referred as f_{c1}, f_{c2} or f_{c3} respectively (centre, left and right).

The mathematical model has to be numerically integrated; we use a time step of 2 ms and a numerical damping of 0.3 for the α-method (HHT). In order to illustrate the simulation of the model a catenary displacement signal is imposed in u_2 (left excitation point) and the angles α_1 and β_1 are plotted to show the slip/stick condition in those degrees of freedom due to Coulomb friction as seen in Fig. 10.

4.1. Optimisation

In order to obtain the optimum parameters that produce the smaller error, several tests have to be carried out and those will be referred to as the training tests, as opposed to the validation test. Nine tests are performed, imposing three different chirp signals (varying in amplitude) over the three different points of the pantograph head.

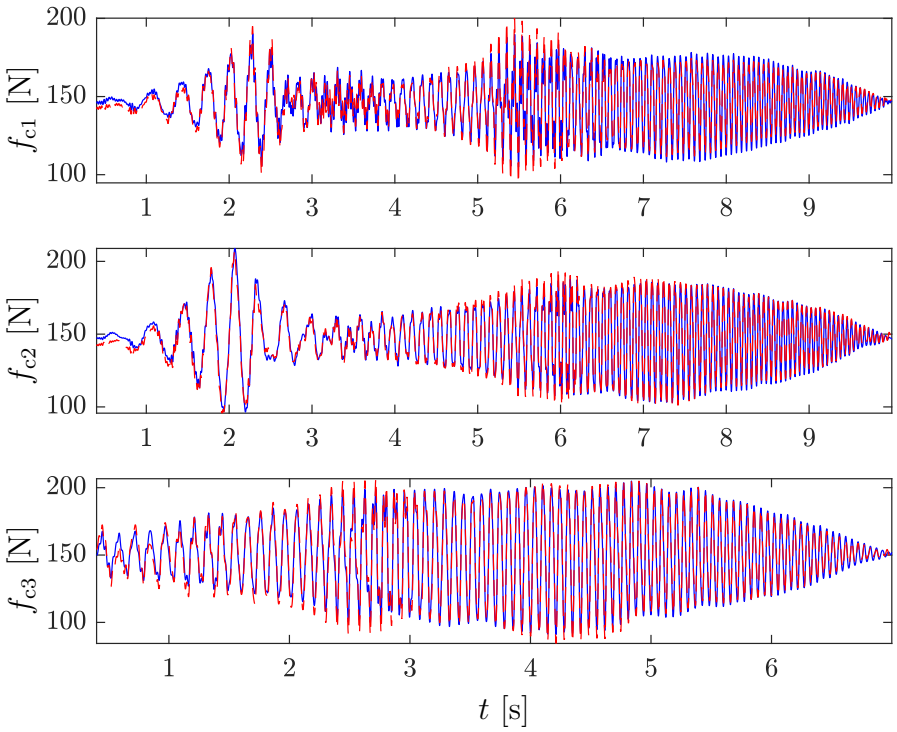


Figure 11: *Training tests for the parameters optimization. Three chirp signasl over the center f_{c1}, left f_{c2} and right f_{c3} point of the pantograh head. Model (Blue solid line) and test (red dashed line).*

A genetic algorithm is employed for the optimisation task. The parameters that yield the minimum root mean square error with respect to the nine tests considered are shown in Tab. 1. The model and measured contact force are shown in Fig. 11 where only three tests are shown to save space and a proper visualisation. The figure shows the similarities between the model and the real pantograph after performing the optimisation.

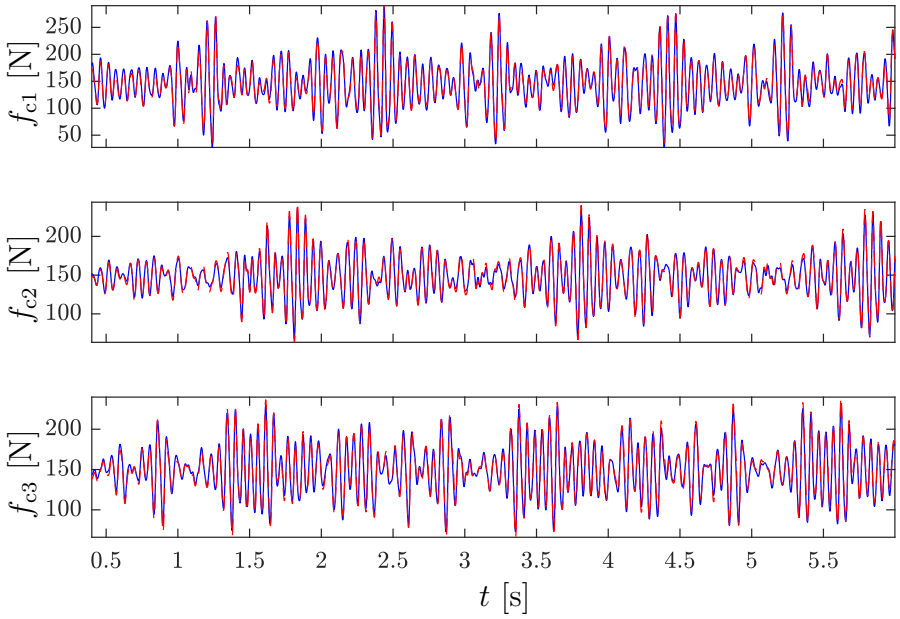


Figure 12: *Validation of the model. Three pseudo signals over the centre f_{c1}, left f_{c2} and right f_{c3} point of the pantograph head. Model (Blue solid line) and test (red dashed line).*

4.2. Validation

The same comparison procedure is employed to validate the optimised model but using different tests that have not been used in the optimisation process. Three tests with pseudo signals over the three excitation points of the pantograph can be observed in Fig. 12 and three tests with the catenary signal in Fig. 13. The tests with the catenary signal are very relevant because the working conditions of the pantograph are the ones expected in a real scenario.

The catenary signal imposed in the tests is the displacement of the contact point obtained from a pantograph-catenary simulation. Particularly, the

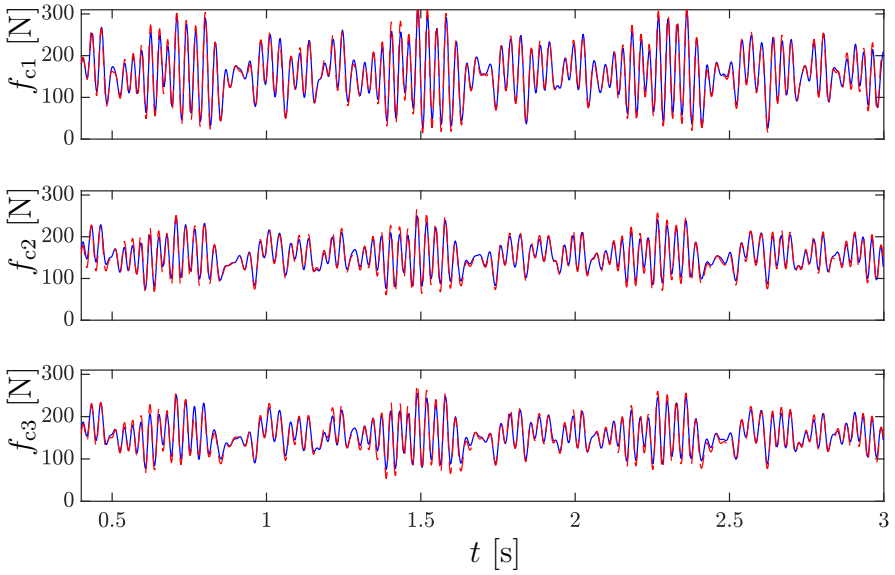


Figure 13: *Validation of the model. Three catenary signals over the center f_{c1}, left f_{c2} and right f_{c3} point of the pantograh head. Model (Blue solid line) and test (red dashed line).*

catenary was periodic so the signal is periodic after a transient zone. Thus the Fourier series can be computed from the contact force, taking the part where it is periodic. In Fig. 14 the frequency content of the contact force obtained from the tests and from the model simulations are compared for the three different excitation points over the pantograph. Note that the frequency content is, in general, bigger when the displacement is imposed at the centre of the pantograph head, hence the bigger amplitude observed in Fig. 13 for the centred excitation.

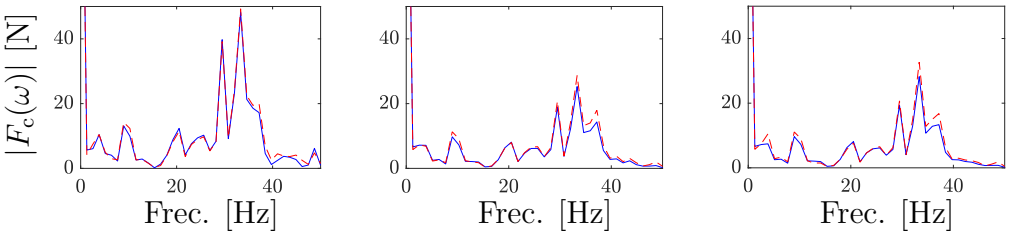
For all the comparisons performed with the model and the test measurements, there is a good agreement in both temporal and frequency domains. The error of temporal series can be quantified by the Mean Absolute Percentage Error (MAPE):

$$\text{MAPE} = \frac{1}{n}\sum_{1}^{n}\left|\frac{f_{\text{c}} - \bar{f}_{\text{c}}}{\bar{f}_{\text{c}}}\right| \tag{16}$$

for a signal of n points where $\bar{f}_{\text{c}}$ is the measured contact force and f_{c} the predicted contact force. The error obtained in the validation process is not bigger than the error achieved in the training due to the fact that enough data is used in the training process. The error is very similar in all the cases tested and the MAPE is always lower than 5%.

5. conclusions

The pantograph model presented in this paper has particular characteristics compared with others in the literature. The combination of non-linear elements with linear elements is a very efficient representation of the pantograph that allows including most of the features of the pantograph with



(a) *Centre excitation* **(b)** *Left excitation* **(c)** *Right excitation*

Figure 14: *Validation of the model. The frequency content of the contact force when catenary displacement is applied over different excitation points. Model (Blue solid line) and test (red dashed line).*

a small number of parameters. The consideration of a three-part oblique spring with friction for modelling the pantograph head springs is crucial to account for the non-linear behaviour of the pantograph. The pantograph model accounts for the flexion of the pantograph head, the asymmetry of the pantograph and the dynamic of eccentric load over the pantograph strips, including the roll movement of the pantograph head and upper frame. Regarding the numerical integration of the model dynamic equation, we have found that implicit integration schemes are slow and implicit integration schemes (which need a non-linear resolution algorithm) do not converge when solving the implicit equation of every time step. A modification of the tangent matrix when using the Newton-Raphson algorithm by altering the derivative of the friction law has been an important proposal to solve this issue. A parameter optimisation has been performed so that the model fits the experimental tests of the pantograph. The model has demonstrated to be accurate in predicting the contact force measured in pantograph tests when a displacement signal is imposed over the pantograph strips. The validation of the model is

performed in tests with a representative excitation of the pantograph catenary interaction tested in three different points of the pantograph head. The Mean Absolute Percentage Error of the predicted contact force in all the cases tested is lower than 5%.

Acknowledgements

The authors would like to acknowledge the financial support received from the State Research Agency of the Spanish Science and Innovation Ministry (PID2020-113458RB-I00) and from the Valencian Regional Government (PROMETEO/2021/046).

References

[1] S. Bruni, J. Ambrosio, A. Carnicero, Y. H. Cho, L. Finner, M. Ikeda, S. Y. Kwon, J. P. Massat, S. Stichel, M. Tur, The results of the pantograph-catenary interaction benchmark, Vehicle System Dynamics 53 (3) (2015) 412–435.

[2] EN 50318:2018, Railway applications. Current collection systems. Validation of simulation of the dynamic interaction between pantograph and overhead contact line, European Union Agency for Railways (2018).

[3] A. Collina, A. Facchinetti, F. Fossati, F. Resta, Hardware in the loop test-rig for identification and control application on high speed pantographs, Shock and Vibration 11 (2004) 445–456.

[4] F. Resta, A. Facchinetti, A. Collina, G. Bucca, On the use of a hardware

in the loop set-up for pantograph dynamics evaluation, Vehicle System Dynamics 46 (S1) (2008) 1039–1052.

[5] A. Facchinetti, M. Mauri, Hardware-in-the-loop overhead line emulator for active pantograph testing, IEEE Transactions on Industrial Electronics 56 (10) (2009) 4071–4078.

[6] A. Schirrer, G. Aschauer, E. Talic, M. Kozek, S. Jakubek, Catenary emulation for hardware-in-the-loop pantograph testing with a model predictive energy-conserving control algorithm, Mechatronics 41 (2017) 17 – 28.

[7] J. Gil, M. Tur, S. Gregori, A. Correcher, A. M. Pedrosa, F. J. Fuenmayor, Hardware-in-the-loop simulations of a railway pantograph with a finite element periodic catenary model, Vehicle System Dynamics 0 (0) (2023) 1–24. doi:10.1080/00423114.2023.2190031.

[8] N. Zhou, W. Zhang, Investigation on dynamic performance and parameter optimization design of pantograph and catenary system, Finite Elements in Analysis and Design 47 (3) (2011) 288–295. doi:https://doi.org/10.1016/j.finel.2010.10.008.
URL https://www.sciencedirect.com/science/article/pii/S0168874X10001782

[9] D. Song, Y. Jiang, W. Zhang, Dynamic performance of a pantograph–catenary system with consideration of the contact surface, Proceedings of the Institution of Mechanical Engineers, Part F: Journal

of Rail and Rapid Transit 232 (1) (2018) 262–274. doi:10.1177/0954409716664934.

[10] W. Wang, Y. Liang, W. Z. S. Iwnicki, Effect of the nonlinear displacement-dependent characteristics of a hydraulic damper on high-speed rail pantograph dynamics, Nonlinear Dynamics 95 (4) (2019) 3439–3464. doi:10.1177/0954409716664934.

[11] J. Ambrósio, F. Rauter, J. Pombo, M. S. Pereira, A Flexible Multibody Pantograph Model for the Analysis of the Catenary–Pantograph Contact, Springer Netherlands, Dordrecht, 2011, pp. 1–27. doi:10.1007/978-90-481-9971-6_1.
URL https://doi.org/10.1007/978-90-481-9971-6_1

[12] A. Wilk, L. Gelman, S. Judek, K. Karwowski, M. Mizan, T. Maciołek, M. Lewandowski, A. Jakubowski, K. Klimowska, Novel method of estimation of inertial and dissipative parameters of a railway pantograph model, Vehicle System Dynamics 60 (7) (2022) 2413–2435. doi:10.1080/00423114.2021.1901942.

[13] M. Zhu, S. Y. Zhang, J. Z. Jiang, J. Macdonald, S. Neild, P. Antunes, J. Pombo, S. Cullingford, M. Askill, S. Fielder, Enhancing pantograph-catenary dynamic performance using an inertance-integrated damping system, Vehicle System Dynamics 60 (6) (2022) 1909–1932. doi:10.1080/00423114.2021.1884273.

[14] J. Pombo, J. Ambrósio, M. Pereira, F. Rauter, A. Collina, A. Facchinetti, Influence of the aerodynamic forces on the panto-

graph–catenary system for high-speed trains, Vehicle System Dynamics 47 (11) (2009) 1327–1347. doi:10.1080/00423110802613402.

[15] D. D. Quinn, A New Regularization of Coulomb Friction , Journal of Vibration and Acoustics 126 (3) (2004) 391–397. doi:10.1115/1.1760564.
URL https://doi.org/10.1115/1.1760564

[16] H. M. Hilber, T. J. R. Hughes, R. L. Taylor, Improved numerical dissipation for time integration algorithms in structural dynamics, Earthquake Engineering & Structural Dynamics 5 (3) (1977) 283–292.